UniScatter: a Metamaterial Backscatter Tag for Wideband Joint Communication and Radar Sensing

Kun Qian, Lulu Yao, Kai Zheng, Xinyu Zhang, Tse Nga Ng

University of California San Diego

ABSTRACT

Millimeter-wave backscatter can simultaneously support high-precision sensing and massive communication and represent one prominent technical evolution in next-generation wireless systems. The backscatter tags should ideally work across a wide mmWave spectrum range with consistent signal strength and angular coverage to accommodate highly diverse application scenarios. However, existing tags made of resonant antennas and RFICs only achieve a few GHz of bandwidth and hardly meet these requirements. In this paper, we present UniScatter, a new backscatter tag structure based on metamaterials. The key design of UniScatter is a graphene-based modulator and a lens-based retroreflector, which have consistent electromagnetic responses across an extensive frequency range and wide angular field-of-view. We have developed a robust fabrication process for UniScatter, and tested it on various mmWave sensing and communication devices. Our field tests show that UniScatter can backscatter signals across a wide frequency band from 24 GHz to 77 GHz with consistently high signal strength and wide angular coverage in 3D space.

CCS CONCEPTS

• **Hardware → Wireless devices**; **Analysis and design of emerging devices and systems**.

KEYWORDS

Millimeter-wave, Backscatter, Metamaterial, Graphene Capacitor, 3D Printing, Luneburg Lens, FMCW Radar

1 INTRODUCTION

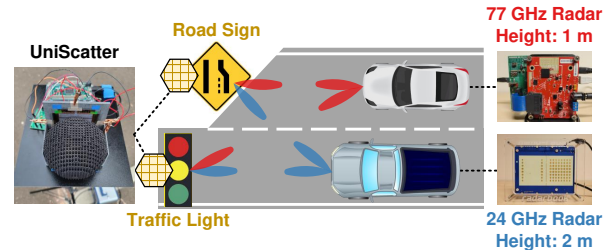Millimeter-wave joint communication and sensing (JCAS)

Figure 1: UniScatter and one of its representative use case, intelligent transportation infrastructure.

is heralding a new technology evolution in next-generation wireless systems [85]. By sharing spectrum and hardware between communication and radar sensing, JCAS can substantially lower the device cost and reduce the form factor while embedding intelligence into network infrastructures. One prominent form of JCAS is radar backscatter communication [7, 15, 43, 59, 75], where a "tag" can convey information to the radar by reflecting and modulating the radar signals. Leveraging the abundant spectrum resources, such radar backscatter communication technologies could simultaneously support high-precision sensing and reliable communication. Considering the ubiquitous deployment of automotive radar and the forthcoming standardization of dual-function radar/radar communication devices [52], such radar backscatter communications could witness a wide range of usage scenarios.

For example, the tag can be installed on roadside infrastructures to facilitate intelligent transportation. It could act as all-weather smart signage to deliver dynamic information to automotive radars without requiring separate transceivers. The tag can also serve as an information kiosk, ubiquitously deployed in grocery stores, urban streets, *etc.*, which can be read by JCAS-compatible devices, such as the 802.11ay WLAN radar [31, 86]. To accommodate the highly diverse application scenarios, the radar backscatter tag should ideally be able to communicate with devices across a wide spectrum range, *e.g.*, to accommodate both 24 GHz and 77 GHz radars or 60 GHz WiGig and 28 GHz 5G/6G mobile devices. The tag size must remain fixed to compensate for the increased path loss at higher frequencies. For example, the path loss is about 10 dB higher at 77 GHz than at 24 GHz. In addition, it should bear a sufficiently wide angular coverage to cater to devices coming from different directions.

Unfortunately, state-of-the-art radar backscatter tags do not yet meet these requirements. Existing tags are commonly built from patch antennas and RFICs. Such RF electronics are fundamentally crippled by the tradeoff curve between *Q*-factor and bandwidth. To ensure the signal loss is acceptable, they can only achieve a few GHz of bandwidth, an order of

magnitude narrower than the ideal use cases. In addition, existing tags adopt retroreflective antenna arrays, such as Van Atta arrays (VAAs) [75] and Rotman lens [20], to retroreflect mmWave signals, but the retroreflection is constrained on a 2D plane. Moreover, the number of antenna elements of a retroreflective antenna array is limited by the wide mmWave bandwidth [64]. Given a fixed number of antenna elements limited by the bandwidth, the size of the tag shrinks with the frequency and cannot compensate for the increased path loss at higher frequencies.

In this paper, we propose UNISCATTER, a reconfigurable metamaterial-based mmWave tag, as a new paradigm to transcend these limitations. UNISCATTER comprises metamaterials with consistent electromagnetic (EM) responses across an extremely wide frequency range. UNISCATTER overcomes the increasing path loss at higher frequencies with a frequency-independent size. Moreover, it has a wide angular field-of-view (FoV), covering both the azimuth and elevation directions. Fig. 1 illustrates how UNISCATTER fits in the use case of intelligent transportation infrastructure. As an ultra-wideband backscatter tag, UNISCATTER can communicate with both 24 GHz and 77 GHz radars on different automotive models. Thanks to the 3D coverage, a single UNISCATTER tag can communicate with radars in different 3D directions, e.g., vehicles at different lanes with different heights.

Designing a wideband radar backscatter tag poses many unique challenges. Such a tag generally consists of two modules, a *modulator* and a *retroreflector*. The modulator modulates the magnitude/phase of the backscatter signals by changing the reflection coefficient of the tag. The retroreflector concentrates signal power into a directional beam backward the radar to compensate for the high attenuation at mmWave frequencies. To realize a wideband modulator, we design a graphene metasurface with uniform reflection coefficients across a wide band from 20 GHz to 90 GHz. Prior research in material science [84] demonstrated that the reflection coefficient of graphene changes with electrochemical doping, i.e., exposing graphene to an electrolyte and applying a bias voltage. However, a large graphene sheet responds slowly to the on/off voltage, resulting in a low modulation rate. We build a distributed circuit model and identify the root cause–the low surface conductivity of graphene. To overcome the hindrance, we coat metallic patterns onto the graphene sheet through a sputtering process. This improves the conductivity and hence modulation rate substantially.

To achieve wideband 3D retroreflection, UNISCATTER uses a Luneburg lens [56] as the retroreflector. Theoretically, Luneburg lens retroreflects signals at any frequency, thanks to its frequency-independent gradient refractive index (GRIN) profile [56], i.e., distribution of permittivity. Unfortunately, the standard Luneburg lens is spherical and cannot be aligned with the flat graphene modulator. To overcome this challenge, we adopt transformation optics (TO) to reshape the spherical lens into a flat-bottom lens while retaining its retroreflectivity. Based on the coordinate transformation between the two lenses, the GRIN profile of the deformed lens can be

obtained. The GRIN profile of the lens is inhomogeneous, and composing natural materials with arbitrary permittivity is extremely challenging. Instead, we discretize the lens into sub-wavelength *unit elements*. Each unit element comprises a tiny 3D printable dielectric structure and the air gap around it. By tuning the dielectric and air ratio, we can achieve arbitrary permittivity for each unit element and construct the entire lens through standard 3D printing.

Fabricating UNISCATTER is not straightforward. We explored various recipes and finally developed robust fabrication processes for both the modulator and the retroreflector. Specifically, modulator fabrication involves graphene transfer, metal coating, modulator assembly, and control circuit assembly. For the retroreflector, we adopt a commercial 3D printing service, i.e., Multi Jet Fusion [77]. We have fabricated UNISCATTER with different modulator configurations. We further conducted extensive field experiments with various mmWave JCAS devices, including a commercial 24 GHz [34] and a 77 GHz automotive radar [81], and a 60 GHz 802.11ay JCAS radar [31]. Our experiments show that UNISCATTER can backscatter signals across a wide frequency band from 24 GHz to 81 GHz, and cover a wide angular range of over 70° in 3D space. UNISCATTER can modulate signals at 100 Hz, which suffices for many application scenarios, such as intelligent transportation infrastructure and information kiosks.

In summary, the main contributions of UNISCATTER are:

(i) We design UNISCATTER, the first metamaterial-based mmWave tag that supports backscatter communication over the ultra-wide mmWave band. UNISCATTER retains consistently high modulation efficiency and retroreflection strength. With a 3D FoV, UNISCATTER can meet the coverage requirement of practical applications more flexibly.

(ii) We develop model-driven optimization solutions to improve UNISCATTER performance to meet the requirement of practical mmWave backscatter. For the modulator, we develop a metal coating scheme to improve the modulation rate. For the retroreflector, we adopt a reshaping scheme to make the classical Luneburg lens compatible with the flat modulator without compromising its retroreflectivity.

(iii) We propose a robust fabrication process for UNISCATTER. Our experiments verify the feasibility and usefulness of UNISCATTER for mmWave radar backscatter communication.

2 RELATED WORKS

MmWave backscatter. Backscatter communication technologies [53, 54] can connect low-power IoT tags to various wireless networks, such as Wi-Fi [37, 95], FM radio [83], LoRa [26, 29, 65], and RFID [57]. Owing to the massive spectrum bandwidth, mmWave backscatter can achieve both high communication efficiency and location resolution. Existing work [15, 40, 78] generally adapts microwave backscatter tag design to the mmWave band. For example, using a 24 GHz automotive radar, MilliMetro [75] can localize mmWave tags at cm-level accuracy, and OmniScatter [7] can identify hundreds of tags in a similar way to RFID. MmTag [59] achieves

1 Gbps backscatter bit rate with a 24 GHz mmWave tag.

However, existing mmWave tags only work at a single frequency band which cannot meet the requirements of the aforementioned applications. The fundamental reason lies in the conventional mmWave antennas, whose achievable bandwidth is less than 10% of the resonating frequency [9], *i.e.*, at most several GHz at mmWave frequencies. Moreover, existing mmWave tags commonly use VAA [30] or Rotman lens [20] to retroreflect signals, to circumvent the sophisticated beam alignment with the directional interrogators. However, these retroreflective antenna arrays have a limited bandwidth due to unequal lengths of signal propagation routes. Specifically, as the signal frequency deviates from the designed frequency, the phase shifts of signals at different antennas diverge, which corrupts the retroreflectivity. Thus, given the bandwidth requirement, the size of these retroreflective structures, and thus their RCS, are severely limited, ultimately limiting their detectability. For example, a VAA for 77 GHz radar can have at most three antenna pairs given the 5 GHz bandwidth [64]. This VAA only has an RCS of -38 dBsm, equivalent to a tiny 1.5×1.5 cm^2 metal reflector. To increase the RCS, existing designs [7, 64, 75] group multiple patch antennas as a single element which, however, reduces the main beam width and scarifies the angular coverage. Last but not least, the RFICs used for signal modulation only have limited bandwidth due to parasitic capacitance. UniScatter transcends the bandwidth and coverage limitations using a metamaterial-based modulator and retroreflector.

Intelligent metasurfaces. Metasurfaces are artificial structures that can abruptly change the propagation properties of EM waves, such as reflection [68, 79, 89], transmission [6, 14, 71], absorption [3, 49], and polarization switch [17, 35, 64]. By deploying metasurfaces to alter ambient wireless signals, a pervasive intelligent environment can be constructed to facilitate communication and sensing. Such metasurfaces can be either passive or active. Passive surfaces can reflect signals towards anomalous directions [68], encode a fixed segment of data into their geometrical shapes [23, 48, 64]. In contrast, UniScatter exploits the metamaterials that can actively switch between states to deliver an arbitrary stream of binary data continuously. Thus, UniScatter can employ frequency modulation schemes to easily filter out the static ambient interference and expand the coding capacity with coding sequences. On the other hand, active metasurfaces are mainly used to facilitate existing wireless communication links through beamforming, polarization matching, or relaying [6, 17, 49, 89]. The UniScatter modulator is essentially an active metasurface, built on a graphene structure and used to convey additional information to radar.

Joint communication and sensing (JCAS). JCAS presents the opportunity for simultaneous high sensing accuracy and large communication capacity, especially with mmWave signals, thanks to their large bandwidth and short wavelength [52, 85, 94]. Integrating two systems into one can achieve more efficient radio spectrum usage while reducing device size, power consumption, and cost. Most works either add the other function to existing communication [41] and sensing systems [70] or jointly design systems from the start with new waveforms [62] and beamformers [51]. Radar backscatter communication [7, 75] extends the scope of JCAS by letting passive targets actively communicate with radars and communication radios. Compared with existing backscatter systems, UniScatter achieves a much wider communication spectrum with a metamaterial-based tag design, which can accommodate more highly diverse application scenarios.

3 UNISCATTER TAG DESIGN

In general, the detection and decoding accuracy of a radar backscatter tag depends on the received signal strength (RSS) variation between different modulation states of the tag, which follows the Friis law:

$$\Delta P_r = \frac{P_t G_t G_r \lambda^2 \Delta \sigma}{(4\pi)^3 d^4}, \tag{1}$$

where P_t, G_t, G_r, λ, and d are the transmit (Tx) signal power, Tx gain, receive (Rx) gain, signal wavelength, and radar-to-tag distance, respectively. $\Delta\sigma$ is the Radar Cross Section (RCS) variation caused by the tag's modulation. RCS measures how large and detectable an object is by the radar. It shows that the backscatter performance depends on the tag's RCS variation $\Delta\sigma$. Recall that the UniScatter tag consists of a modulator and retroreflector. So its $\Delta\Sigma$ can be further factorized as:

$$\Delta\sigma = \Delta\Gamma \sigma_m, \tag{2}$$

where σ_m is the maximum RCS of the retroreflector and $\Delta\Gamma$ is the variation of reflection coefficient due to the modulator.

Eq. (2) implies that the tag should retain consistently high $\Delta\Gamma$ to support the whole ultra-wide mmWave band. Besides, according to Eq. (1), the RSS variation decreases with the square of the signal frequency. The tag must compensate for this frequency loss with increasing RCS. In what follows, we introduce the design of the UniScatter modulator (Sec. 3.1) and the retroreflector (Sec. 3.2) to meet these requirements. We also introduce how to detect the tags using standard signal processing on mmWave radar or JCAS devices (Sec. 3.3).

3.1 Modulator Design

3.1.1 Choices of Modulating Materials. To manipulate RF signals as they are reflected by a surface substrate, various tuning mechanisms have been studied in the literature [1, 28, 82]. Considering the commercial availability and fabrication difficulty, we mainly investigate four types of reconfigurable materials, *i.e.*, RF diodes and switches [7, 59, 75], nematic liquid crystal (LC) [21, 58, 91], piezoelectric materials [2, 24, 67], and graphene [10, 39, 45].

RF diodes and switches modulate wireless signals by creating impedance mismatch between RF circuits and antennas [7, 59, 75]. As a result, varying reflection coefficients are applied to re-radiated signals, thus modulating their magnitudes. However, due to parasitic capacitance, these transistor-based modulators have limited operational bandwidth, out of which signals can experience significant loss. Besides, a diode or switch usually controls a small number of antenna
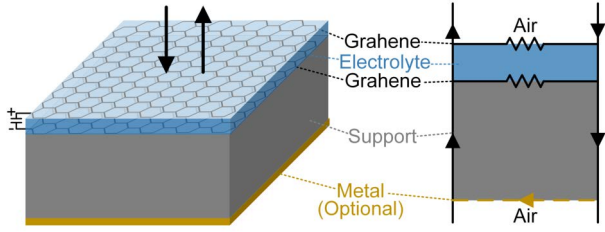
Figure 2: Model of the graphene modulator.

Figure 3: RF reflection property of graphene modulator. (a) Reflection coefficient. (b) Reflection loss.

elements. A mmWave tag with sufficient RCS requires hundreds or even thousands of antenna elements. Thus, a large number of diodes/switches and complex multi-layer wire routing make it challenging to fabricate.

Nematic LC has electrically tunable permittivity due to its rod-shaped molecules. By sandwiching an LC cell between two electrodes and applying bias voltages, the orientations of LC molecules vary between the perpendicular and the parallel state, resulting in a continuous change of permittivity. LC has been used in reconfigurable antennas [58]. However, these antennas only work within a limited bandwidth around the resonant frequency. A simple LC cell could be used for wideband reconfiguration. However, the permittivity variation of common LC is less than 1 [91], and the LC cell thickness is usually at the μm level. At frequencies with mm-level wavelength, the phase shifts introduced by LC cells are too small to separate different modulation states.

Piezoelectric materials create mechanical displacements upon applying electrical fields, known as the converse piezoelectric effect. However, with micrometer-level displacements, piezoelectric transducers cannot generate sufficient EM variations for mmWave backscatter communication [66].

Graphene is a 2D nanomaterial with only one carbon atomic layer. By applying electrochemical doping, i.e., exposing graphene to an electrolyte and applying a bias voltage [84], the resistivity of graphene can be tuned. Graphene has been exploited as the tunable component in a wide range of RF devices, such as antennas [39, 60], diodes [45], and metasurfaces [88, 93], at mmWave and THz bands. However, these designs are either confined to 2D or have limited fractional bandwidth. In contrast, UNISCATTER uses a simpler graphene capacitor structure [10] to achieve wideband reconfigurability (Sec. 3.1.2). With large graphene sheets available [74], UNISCATTER can easily scale up to provide sufficient RCS for mmWave backscattering. UNISCATTER further explores novel metasurface structures to achieve wideband and fast modulation (Sec. 3.1.3).

3.1.2 Graphene Modulator. To tune the surface resistivity of graphene, we apply the electrochemical doping by sandwiching a layer of ionic liquid electrolyte between two graphene sheets, as shown in Fig. 2. The sandwich structure forms a parallel plate *capacitor*, where the two graphene sheets act as conductive plates and the electrolyte is the dielectric. With different bias voltages applied to the graphene sheets, the density of high mobility charge carriers on the graphene is changed, which varies their surface resistances. The elec-
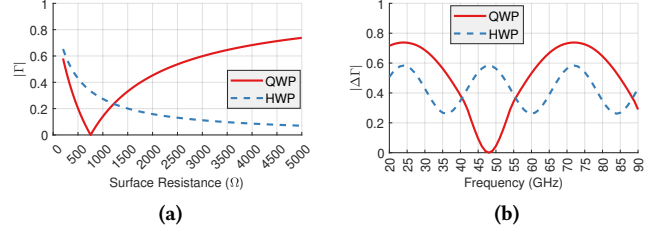
trolyte layer is formed by a thin optical tissue (about 50 μm) soaked with electrolyte, whose impact on mmWave signals is negligible. Meanwhile, the graphene sheets must attach to a substrate to be robust for fabrication and deployment. We use laminating films as the substrates for both graphene sheets. These laminating films are only about 80 μm thick, which has a negligible impact on the interrogating mmWave signals. Thus, the transmission line model of the whole graphene capacitor can be approximated by two variable resistors with resistance Z_g, contributed by two graphene sheets.

The graphene capacitor is flexible and must be attached to a rigid *support*, such as plastics, for a stable modulation effect. The support also impacts the reflection coefficient of the modulator. In the transmission line model, the support can be characterized by its thickness t_s and characteristic impedance Z_s. Finally, an additional *load* can be attached to the bottom of the support, introducing an additional resistance Z_l. For example, as shown in Fig. 2, when a metal ground is used, $Z_l = 0$. When nothing is attached, Z_l is the impedance of free space, i.e., $Z_0 \approx 376.73$ Ω.

Consider all the components, the input impedance of the UNISCATTER modulator is the parallel impedance of the two graphene layers and the input impedance at the upper surface of the support Z_d, i.e.:

$$Z_i = \frac{1}{\frac{2}{Z_g} + \frac{1}{Z_d(f)}} = \frac{Z_g Z_s Z_l + i Z_g Z_s^2 \tan(kt_s)}{Z_s(Z_g + 2Z_l) + i(Z_g Z_l + 2Z_s^2)\tan(kt_s)},$$
(3)

where $Z_d = Z_s \frac{Z_l + i Z_s \tan(kt_s)}{Z_s + i Z_l \tan(kt_s)}$ following the lossless transmission line model, and $k = \frac{2\pi}{\lambda}$ is the wave number. Thus, the reflection coefficient of the modulator is $\Gamma(f) = \frac{Z_i(f) - Z_0}{Z_i(f) + Z_0}$.

The model implies that the reflection coefficient of the modulator is controlled by two parameters, i.e., the support thickness t_s and the load impedance Z_l. Given the specific use cases, we can tune these two parameters to achieve the maximum variation of the reflection coefficient (i.e., $\Delta\Gamma$) across the required frequency bands, in order to optimize the tag's decoding performance, according to Eq. (2). We elaborate on such design choices through example use cases.

To begin with, we consider a single carrier frequency. If no load is applied, i.e., $Z_l = Z_0$, $\Delta\Gamma$ is maximized when $t_s = \frac{\lambda}{2}$. In this case, the support is known as a half-wave plate (HWP). As shown in Fig. 3a, the reflection coefficient with HWP varies between 0.65 and 0.07 (i.e., $\Delta\Gamma = 0.58$), as Z_g varies between 200 Ω and 5,000 Ω. If a metal ground is applied
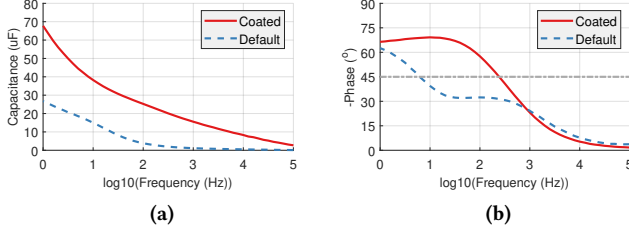
Figure 4: Performance of the graphene capacitor. (a) Effective capacitance. (b) Phase angle.

as the load, *i.e.*, $Z_l = 0$, a local minimal reflection coefficient appears and approaches 0 as $t_s = \frac{\lambda}{4}$. In this case, the support is known as a quarter-wave plate (QWP). As shown in Fig. 3a, a larger $\Delta\Gamma$ of 0.74 is achieved with the QWP.

Then, we consider the performance of the modulator across a wide band, *e.g.*, from 20 GHz to 90 GHz, given the QWP and the HWP designed at 24 GHz. As shown in Fig. 3b, while the QWP achieves higher $\Delta\Gamma$ at most frequencies, $\Delta\Gamma$ drops to 0, and backscatter fails around the even multiples of 24 GHz (*e.g.*, 48 GHz). In contrast, despite smaller $\Delta\Gamma$ on average, the HWP achieves relatively consistent $\Delta\Gamma$ across the whole frequency band from 20 GHz to 90 GHz.

Based on the frequencies of the use cases, we can choose different configurations. For example, to communicate with both 24 GHz and 77 GHz automotive radars, we can use the QWP at 24 GHz for higher $\Delta\Gamma$. In contrast, to communicate with both 5G mmWave (28 GHz) and WiGig (60 GHz) JCAS devices, a QWP at 28 GHz results in almost zero $\Delta\Gamma$ at 60 GHz. Instead, the HWP at 28 GHz is a better choice.

3.1.3 Modulation Optimization. The graphene modulator can modulate signals by switching between different states. The switching rate is a crucial metric. First, it determines the maximum modulation bitrate of the tag. Second, in dynamic scenarios, *e.g.*, when UNISCATTER acts as an intelligent road sign for moving vehicles, the switching rate must be sufficiently high to ensure the tag's Doppler spectrum is separable from the object's.

The switching rate is essentially limited by the transient delay of the graphene capacitor. To characterize this, we fabricate a 5×5 cm^2 graphene capacitor (Sec. 4.1) and conduct an electrochemical impedance spectroscopy (EIS) measurement with a potentiostat [11]. Fig. 4a shows the effective capacitance of the graphene capacitor as the switching rate varies between 1 Hz and 100 Hz. The capacitance of the original graphene capacitor decreases dramatically from 27 μF at 1 Hz to only 4 μF at 100 Hz, indicating that most portion of the graphene capacitor does not take effect. As a result, the surface resistances of the graphene sheets are not fully changed to generate the theoretical maximum $\Delta\Gamma$, resulting in a low-efficiency modulator.

The response time of a capacitor can be characterized by its phase angle, where a larger phase angle represents a faster response. Generally, the phase angle of a capacitor decreases as frequency increases due to the existence of the
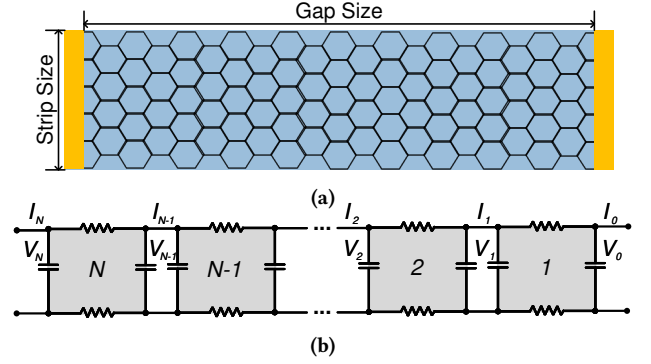

Figure 5: Model of the graphene capacitor. (a) Top view of a graphene capacitor. (b) Equivalent distributed-element circuit of the capacitor.

internal resistance [87]. The phase angle of 45° indicates the cutoff frequency, only below which most portion of the capacitor takes effect. It also determines the switching rate of the graphene modulator. As shown in Fig. 4b, the cutoff frequency of the default graphene capacitor at 45° is less than 10 Hz, indicating a low modulation efficiency.

To figure out the root cause, we model the large graphene capacitor with a distributed-element circuit. Fig. 5a shows the top plate of the graphene capacitor. Two metal strips (golden) on the opposite edges of the graphene sheet connect the plate to one of the electrodes of the power source. For clarity, we denote the distance between the two source strips as the *gap size* and the length of the strips as the *strip size*. Fig. 5b shows the circuit model of the whole graphene capacitor. Specifically, we split the whole graphene sheets into N segments in series. Each segment can be modeled by a two-port network consisting of the resistors R of the two graphene pieces and the capacitor C between them. We denote the input voltage and the current injection of the k-th two-port network as V_k and I_k, respectively.

Then the transmission matrix of the k-th two-port network can be formulated as follows:

$$\begin{bmatrix} V_k \\ I_k \end{bmatrix} = \mathbf{T} \begin{bmatrix} V_k \\ I_k \end{bmatrix}, \mathbf{T} = \begin{bmatrix} i\omega CR + 1 & 2R \\ -\frac{\omega^2 C^2 R}{2} + j\omega C & j\omega CR + 1 \end{bmatrix}, \quad (4)$$

where ω is the frequency of the power source applied to the circuit. According to Eq. (4), we have the relations $\begin{bmatrix} V_N \\ I_N \end{bmatrix} = \mathbf{T}^N \begin{bmatrix} V_0 \\ I_0 \end{bmatrix}$. Meanwhile, we assume the power source connects to both ends of the capacitor, which provides the boundary conditions $V_N = V_0 = V_s$. Thus, we can solve for the circuit parameters I_N and I_0. According to Kirchhoff's circuit laws, the impedance of the whole capacitor is $Z_c = \frac{V_N}{I_N - I_0}$.

The foregoing model allows us to examine the capacitor design through numerical simulation. For clarity, we denote the length between the two source poles as the *gap size* and the length of the strips as the *strip size*. Fig. 6a shows the phase angle of the capacitor with respect to the gap/strip size at 100 Hz. While the strip size has a minor impact on the phase angle, the gap size impacts the phase angle significantly. When the gap size is smaller than a threshold
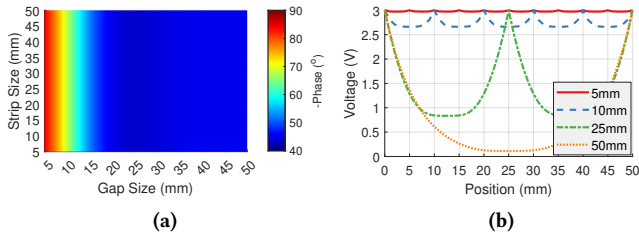
Figure 6: Simulation results of graphene capacitor. (a) Phase angle of the capacitor. (b) Voltage distribution along the graphene sheet.

(*e.g.*, 15 mm in Fig. 6a), the whole capacitor becomes fully charged as the gap size reduces. However, when the gap size exceeds the threshold, the portion of the capacitor that is more than half of the threshold away from the source poles is not charged at all, and the phase angle reduces below 45°.

Fig. 6b further shows the voltage distribution along the graphene capacitor with different gap sizes. When the gap size is 50 mm, the central part of the capacitor has nearly zero voltage, leading to a negligible modulation effect. When the gap size is reduced to 5 mm, the voltage variation of the whole capacitor remains close to the source voltage, *i.e.*, 3V.

The foregoing model indicates that *a smaller gap size is required to achieve a higher switching rate*. We propose to coat metal wires on the graphene sheets (Sec. 4.1) to reduce the gap size while retaining the total size of the graphene capacitor. The metal wires distribute equally between the two source poles and also connect to the source, as illustrated in Fig. 11a. Thus, the part of the graphene capacitor that is far away from the source poles now becomes close to the metal wires and thus can be charged faster. Fig. 4 shows the capacitance and phase angle of the metal-coated graphene capacitor. It has a much larger capacitance than the original capacitor and achieves a cutoff frequency of over 100 Hz. In other words, it can achieve a switching rate of 100 Hz, which can provide sufficient modulation bitrate and separation between the Doppler spectrum of the tag and the object, given that the common Doppler peak width is less than 50 Hz [69].

3.2 Retroreflector Design

3.2.1 Design Choices for Retroreflectors.

Retroreflectors reflect EM waves back to the incident direction. Considering the frequency, bandwidth, angular coverage, and scalability of RCS, we mainly investigate four types of retroreflectors, *i.e.*, Van Atta array (VAA) [73], trihedral corner reflector [19], cat's eye retroreflector [63], and Luneburg lens [56]. The VAA is ruled out due to the aforementioned bandwidth and coverage limitations (Sec. 2).

A trihedral corner reflector consists of three electrically conductive surfaces, which are welded at an angle of 90°. Incoming EM waves are retroreflected after specular reflections from three surfaces consecutively. The trihedral corner reflector applies to any frequency and can arbitrarily scale up its dimensions to increase RCS. But it only has limited angular coverage of about 50° [44]. More importantly, in-

tegrating it with the graphene modulator is challenging. A simple assembling method is to replace one surface of the corner reflector with the graphene modulator. However, the $\Delta\sigma$ reduces to zero as the signal's incident direction deviates from the modulator's normal direction, resulting in an even smaller angular coverage of the tag.

A cat's eye retroreflector consists of a convex lens and an electrically conductive mirror at the focal plane. With the mirror's specular reflection and the lens's forward-backward refraction, incoming signals can be retroreflected. Such a retroreflector could be integrated with the graphene modulator by simply replacing the mirror with the modulator. However, the angular coverage of a cat's eye lens depends on the permittivity of the lens [63]. Using plastics with low permittivity, the angular coverage of the lens is quite small (*e.g.*, < 40°). Whereas a lens with large permittivity increases the angular coverage, it also has a large reflection coefficient, leading to an additional insertion loss and hence the attenuation of the incoming signals.

A Luneburg lens is a spherically symmetric gradient-index lens [56] with permittivity profile $\varepsilon(r) = 2 - (\frac{r}{R})^2$, where R is the radius of the lens, and r is the distance of any point to the sphere center. The Luneburg lens has consistent RF responses at all frequencies due to the frequency-independent permittivity profile. The radially decreasing permittivity profile turns any surface point of the Luneburg lens into a focal point. The Luneburg lens has been exploited for designing beamforming antennas [42, 46, 50] and reshaped to align with flat antenna arrays [12, 33, 47]. UNISCATTER adopts the Luneburg lens as the retroreflector, where the lens is reshaped to have a flat-bottom focal plane to align with the reflective graphene modulator surface.

3.2.2 Flat-Bottom Luneburg Lens.

To reshape the Luneburg lens into a flat-bottom lens while retaining its retroreflectivity, we adopt the transformation optics (TO) method [61, 72]. Intuitively, TO can reshape a geometrical structure with the coordinate transformation between the source and target coordinate spaces:

$$\begin{bmatrix} u \\ v \end{bmatrix} = \mathbf{A}(x, y) \begin{bmatrix} x \\ y \end{bmatrix}, \mathbf{J} = \begin{bmatrix} \frac{\partial u}{\partial x} & \frac{\partial u}{\partial y} \\ \frac{\partial v}{\partial x} & \frac{\partial v}{\partial y} \end{bmatrix}. \tag{5}$$

where (x, y) and (u, v) represent the coordinates in the source and the target spaces. $\mathbf{A}$ is the coordinate-dependent transformation matrix. $\mathbf{J}$ is the Jacobian matrix of the transformation.

To retain the EM propagation characteristics of the original structure, the impact of coordinate transformation can be compensated by modifying the permittivity $\mathbf{E}$ and permeability $\mathbf{M}$ profiles in the target space:

$$\mathbf{E}'(u, v) = \frac{\mathbf{J}\mathbf{E}(x, y)\mathbf{J}^T}{|\mathbf{J}|}, \mathbf{M}'(u, v) = \frac{\mathbf{J}\mathbf{M}(x, y)\mathbf{J}^T}{|\mathbf{J}|}, \tag{6}$$

For clarity, we define the longitudinal axis of the Luneburg lens as the z-axis. Fig. 7a shows the standard spherical Luneburg lens and its permittivity profile in the x-z plane. Note that the permittivity of the 3D lens is symmetric to the z-axis. Fig. 7b shows the target flat-bottom structure. The
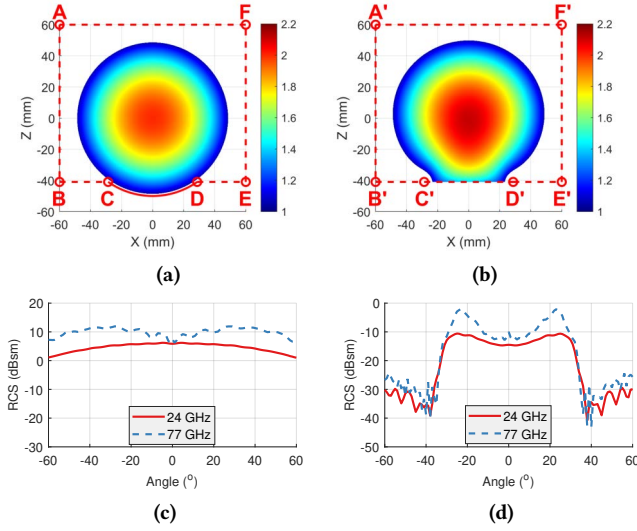
(a) **(b)**

(c) **(d)**

Figure 7: Modification of Luneburg lens. Permittivity profile of (a) default Luneburg lens, and (b) flat-bottom Luneburg lens. Monostatic RCS of (c) default Luneburg lens, and (d) flat-bottom Lunburg lens.

target structure's permittivity matrix can be calculated once the coordinate transformation **A** is known.

Unfortunately, a coordinate transformation between sophisticated structures as such usually does not bear an analytical form. Instead, we find **A** numerically by solving the Laplace's equations:

$$\frac{\partial^2 x}{\partial u^2} + \frac{\partial^2 x}{\partial v^2} = 0, \; \frac{\partial^2 y}{\partial u^2} + \frac{\partial^2 y}{\partial v^2} = 0, \qquad (7)$$

with zero and first-order boundary conditions [32]:

$$(u, v)|_{\text{A'B', E'F', F'A'}} = (x, y)|_{\text{AB, EF, FA}},$$
$$(u, v)|_{\text{B'C', D'E'}} = (x, y)|_{\text{BC, DE}}, \; (u, v)|_{\text{C'D'}} = (x, y)|_{\widehat{\text{CD}}},$$
$$\frac{\partial x}{\partial v}|_{\text{A'F'}} = \frac{\partial x}{\partial v}|_{\text{B'C'}} = \frac{\partial x}{\partial v}|_{\text{D'E'}} = 0, \qquad (8)$$
$$\frac{\partial y}{\partial u}|_{\text{A'B'}} = \frac{\partial y}{\partial u}|_{\text{E'F'}} = 0.$$

The result guarantees that the solution is derivable everywhere, *i.e.*, the Jacobian matrix **J** always exists, as required by calculating the modified permittivity profile using Eq. (6).

The Laplace equations can be solved by the iterative finite difference method [13]. The solution is a numerical inverse coordinate transformation $\mathbf{A}^{-1}:(u, v) \rightarrow (x, y)$, from which **A** can be obtained. Given **A**, the numerical Jacobian matrix **J** can be calculated, and the permittivity profile **E'** can be obtained according to Eq. (6). Fig. 7b shows the 2D permittivity profile within the vertical cross-section of the flat-bottom Luneburg lens. The 3D permittivity profile can be obtained by rotating the 2D profile around the central axis of the lens.

For the UNISCATTER prototype, we set the arc CD to $70°$. Correspondingly, the flat-bottom Luneburg lens has an angular coverage of $70°$, which is sufficient to cover unidirectional lanes in the transportation use case. The angular coverage can be further increased by increasing the length of the arc CD, at the cost of a larger modulator. The trade-off has to be made according to specific application scenarios. To verify
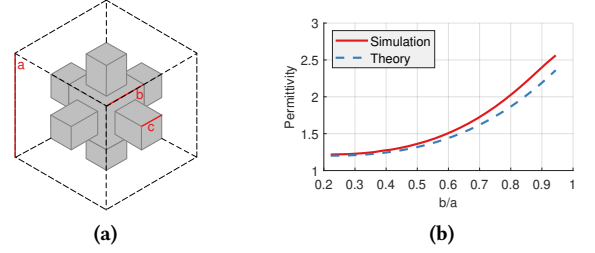

(a) **(b)**

Figure 8: Element design for 3D printing Luneburg lens. (a) Model. (b) Effective permittivity.

the effectiveness of this model-driven design, we conduct finite-difference time-domain (FDTD) simulations for both the standard and the flat-bottom Luneburg lenses using EM-Pro [38]. Since the continuously varying permittivity profiles of the lenses cannot be modeled in numerical simulations with finite precision, we need to segment the lenses into small units with uniform permittivity. Specifically, the standard lens is divided into a series of shells, each of which has uniform permittivity determined by the radius of the shell. A hemispherical metal shell is coated on the opposite side of the incoming EM waves. The flat-bottom lens is discretized into small cubes, each characterized by the permittivity at its geometrical center. A flat metal ground is placed at the bottom of the lens. Fig. 7c and Fig. 7d compare the monostatic RCS pattern of the two lens structures. The standard Luneburg lens has omnidirectional coverage. The flat-bottom lens has a consistent angular coverage of about $70°$ by design across a wide frequency band, *e.g.*, 24 GHz and 77 GHz. If needed, the angular coverage of the flat-bottom lens can be further increased by increasing the arc CD.

3.2.3 3D Printing Luneburg Retroreflector. Fabricating the flat-bottom Luneburg lens is not straightforward in practice, due to the delicate structures and the continuously changing permittivity within the 3D shape. We circumvent this problem by approximating the lens using a single material with uniform permittivity, which is thus 3D printable [8, 46, 50].

First, the continuously changing permittivity profile of the flat-bottom Luneburg lens must be discretized for practical fabrication. Similar to the FDTD simulation (Sec. 3.2.2), the flat-bottom lens is discretized into small cubes, each characterized by the permittivity at its geometrical center.

Then, each cube with specific permittivity must be approximated with a unit element structure that consists of a single material. Although the unit element is inhomogeneous, it can be treated as a homogeneous medium filling the entire cube, as long as the cube size is smaller than half-wavelength in the material [36]. Therefore, *the size of the unit element determines a cutoff frequency, below which the lens always has retroreflectivity*. At this scale, the effective permittivity of the unit element is the average permittivity of the material and the air weighted by their respective volume ratio [50]:

$$\hat{\varepsilon} = (1 - \alpha)\varepsilon_a + \alpha\varepsilon_m, \qquad (9)$$

where $\varepsilon_a = 1$ and ε_m are the permittivities of the air and the material. α is the volume ratio of the material.
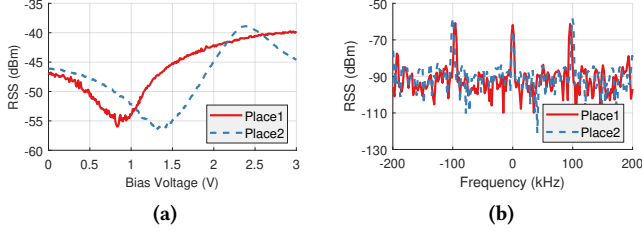
Figure 9: Modulation scheme. (a) Amplitude shift keying. (b) Frequency shift keying.

We adopt a 3D crossing structure as the unit element. As shown in Fig. 8a, the six rods with fixed size c connect the element to adjacent elements. The small central cube with tunable size b controls the effective permittivity. We simulate the S parameters of the structure in Ansys HFSS [4] and derive its permittivity [18]. Fig. 8b shows the theoretical permittivity calculated according to Eq. (9) and the simulated permittivity, which match each other within the tuning range of the central cube size b. By generating crossing structures for all discretized cubes, we have a structure made of a single material, thus suitable for 3D printing.

3.3 Modulation and Detection

3.3.1 Modulation Scheme. UNISCATTER modulates the amplitude/phase of the backscatter signal by applying different bias voltages to the graphene capacitor. A straightforward modulation scheme is amplitude shift keying (ASK), where several amplitude levels are used to represent different symbols. However, the amplitude of the received signal at the radar depends on not only the backscatter signal from the tag but also reflections from surrounding objects. Fig. 9a shows the RSS from UNISCATTER at two different places. Specifically, we increase the bias voltage of the modulator from 0 to 3V at a rate of 0.1 V/s and use a 24 GHz radar to measure the RSS. At place 1, ambient reflections are weak, so the RSS variation follows the theoretical $\Delta\Gamma$ (Fig. 3a). However, at place 2, due to stronger ambient reflections, the trend of the RSS is distorted significantly. This experiment implies that ASK will fail under practical channel dynamics, *e.g.*, when the radar moves in a multipath-rich environment.

Instead, we find that frequency shift keying (FSK) is more robust against strong ambient reflections. Specifically, we configure UNISCATTER to switch between two reflection states at a predefined rate, *e.g.*, 100 Hz. Accordingly, the backscatter signal will experience a positive/negative frequency shift at the switching rate. A mmWave radar can thus separate the backscatter signal from ambient reflections in the Doppler frequency spectrum. Fig. 9b shows the Doppler frequency spectrum of the tag. Here the bias voltage of the modulator is switched between 0.5 V and 3V at a rate of 100 Hz. The peaks of the backscatter signal (coding peaks) are obviously separated from the peak of the ambient reflections (carrier peak). While the ambient reflection changes between places, the doppler spectrum of the backscatter signal remains consistent. Thus, UNISCATTER adopts FSK as the
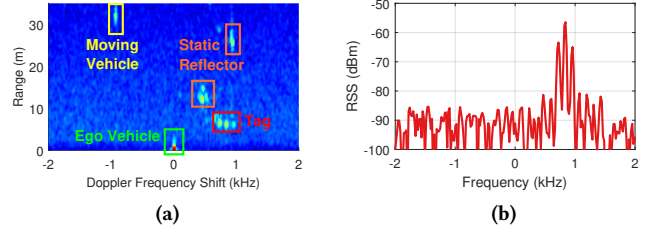

Figure 10: Tag detection. (a) Range Doppler profile of Radar. (b) Doppler frequency spectrum of a tag.

modulation scheme. It maps each data bit to an FSK symbol and switches the modulator to generate the symbol at the predefined frequency, *i.e.*, 100 Hz. The radar can detect the frequency shifts in the Doppler frequency spectrum, convert them into FSK symbols and map them back to data bits.

3.3.2 Tag Detection and Demodulation. Backscatter communication with UNISCATTER can be directly implemented into existing JCAS devices without hardware modification. We take mmWave FMCW radar as an example. To begin with, a mmWave FMCW radar transmits successive chirps with equal time intervals and receives the echoes from the tag and surrounding objects. The radar first applies 1D Fourier transform to each received chirp to obtain the range profile. Then, it applies a second 1D Fourier transform to the range profiles of successively received chirps to obtain the 2D range-Doppler profile. Note that the relative movement between an object and the radar creates non-zero Doppler frequency shifts. Thus, a prominent peak in the range-Doppler profile corresponds to an object at a specific distance and with a specific relative speed. Fig. 10a shows an example of the range-Doppler profile generated by a moving automotive radar, where the hood of the ego vehicle, some static objects, a moving vehicle, and a tag are visible.

Next, the radar applies the 2D constant false alarm rate (CFAR) detection to the range-Doppler profile to identify all prominent peaks. For each peak, it aggregates the measurements across multiple receiving antennas to estimate the angle of arrival (AoA) of the peak. With both the range and the AoA, an object can be detected and localized in the 2D horizontal space. For a typical automotive radar, all the detection results are fed into a multi-object tracker to keep tracking the surrounding objects.

To decode the UNISCATTER backscatter signals, no modification to the standard processing flow is needed. Instead, the system can fetch all detected peaks and their Doppler frequency spectrum from the radar. Then it can *separate the tag from other objects with matched filtering*. Fig. 10b shows the Doppler frequency spectrum of the tag. In contrast to the static tag (Fig. 9b), the whole spectrum only shifts by the Doppler offset between the moving radar and the tag, while the spacing between the coding peaks and the carrier peak does not change. Thus, given the predefined switching rate of the tag, a Doppler frequency template can be generated. The maximum cyclic cross-correlation value between the
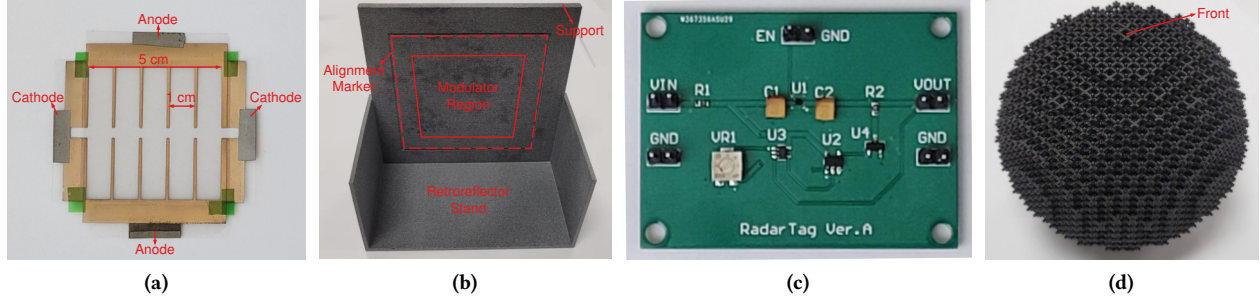
Figure 11: Implementation of UNISCATTER. (a) Graphene capacitor. (b) Stand. (c) Power management circuit. (d) 3D printing flat-bottom Luneburg lens.

template and the Doppler frequency spectrum of each detection can be used as an indicator to detect the tag. Similar to standard radar processing, a separate tracker can be allocated to track the tags. The modulated frequency shifts of the tag can be extracted from its Doppler frequency spectrum and demodulated as FSK symbols.

The same process is applicable when a communication device is used as the interrogator. The channel impulse response (CIR) measurements from such devices are equivalent to the range profiles of radars [25]. So the above demodulation workflow can be applied similarly.

4 IMPLEMENTATION

4.1 Graphene Modulator

We now discuss the fabrication process of the three key components in the graphene modulator, *i.e.*, the graphene capacitor, support, and power source, as modeled in Fig. 2.

4.1.1 Graphene capacitor. Commercial monolayer graphene is grown on copper foil via chemical vapor deposition and sold with the copper foil [16]. So we need to transfer the graphene from the copper foil to 3 mil laminating film, using a high-temperature lamination method [74]. Specifically, the copper foil with single-layer graphene is placed on a piece of laminating film, where the adhesive layer of the film contacts the graphene. Then, two paper sheets cover the top and bottom of the sample to ensure uniform pressure. Next, the sample slowly passes through a laminator at 110 °C. During the lamination, the adhesive layer melts and forms a strong binding with the graphene. After cooling down to room temperature, the laminating film and the copper foil bind together with the graphene sandwiched in between.

Next, the sample is treated with an ultraviolet ozone cleaner for 10 minutes to remove the graphene residue on the other side of the copper foil. Then the sample is cut into the desired size and immersed in 0.5M $FeCl_3$ solution to dissolve the copper foil. After the copper foil is fully dissolved, the laminating film with the graphene is washed with deionized water, and isopropyl alcohol to further remove the residual Fe^{3+}, Fe^{2+}, and Cu^{2+} ions, and dried at room temperature.

The sample is then coated with metal, following the design in Sec. 3.1.3. We use an electron beam evaporator [80] to coat a 50 nm metal layer on the graphene at a deposi-

tion rate of 0.05 nm/s. We select gold for its stability against oxidation. The metal coating has a comb pattern with the teeth separated by the gap size, as discussed in Sec. 3.1.3. E-beam evaporator deposits metal atoms uniformly at the target platform. To confine metal coating to the desired regions, we fabricate metallic shadow masks where only the coating region is hollowed out.

The capacitor is fabricated by using top graphene as the cathode, two optical tissues as the separator, and bottom graphene as the anode. The ionic liquid, Diethylmethyl(2-methoxyethyl)ammonium bis(trifluorometnylsulfonyl)imide [deme][Tf2N], is used as the electrolyte due to the low vapor pressure and high stability in the atmosphere. Finally, we fix the four corners of the two laminating films to each other with tape. Using a potentiostat to measure the cyclic voltammogram of the capacitor, we confirm that the capacitor can work stably within a 3V potential window in the atmosphere.

While the fabrication involves heavy manual operations, we only find minor non-uniformity in the finished graphene capacitors. The variation comes from the quality of transferred graphene, whose measured resistance at 0 V ranges around several kΩ. Nonetheless, we find that its impact on the modulation depth of the graphene capacitor is minor since the reflection coefficient variation diminishes as the surface resistance becomes very large, as in Fig. 3a. Fig. 11a shows a finished graphene capacitor. The effective area of the capacitor is 5×5 cm^2. It can be easily resized according to the size of the lens and the target angular coverage. Based on the simulation result in Fig. 6a, the gap size is set to 1 cm to ensure the capacitor operates at a switching rate of 100 Hz. Using a potentiostat to measure the cyclic voltammogram of the capacitor, we confirm that the capacitor can work stably within a 3V potential window in the atmosphere. One graphene capacitor costs about $175, mainly due to the under-commercialization of graphene. The material costs of electrolyte and gold are $15 and $0.4, respectively.

4.1.2 Deploying the UNISCATTER Tag. We use a stand as the support for the modulator and the holder for the retroreflector. We 3D print two stands with different support configurations, *i.e.*, the QWP and the HWP at 24 GHz, as analyzed in Sec. 3.1.2. The 3D printing material is Nylon 12, with an approximate permittivity of 2.6 between 20 GHz and 100 GHz. Fig. 11b shows the front view of the stand. A rectangular
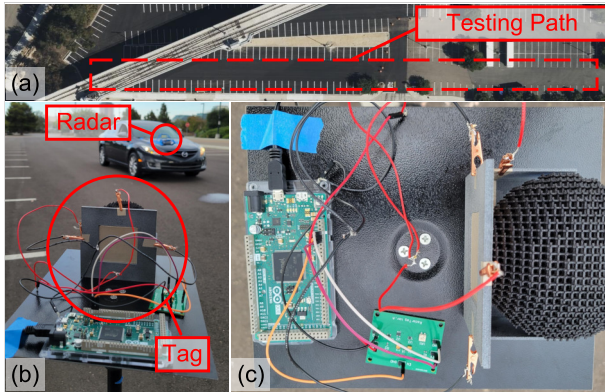
Figure 12: Experimental setup. (a) Bird's eye view of the testing parking lot. (b) Setup for the automotive driving scenario. (c) Assembling of UNISCATTER.

marker is carved on the support for alignment with the capacitor. At the back of the QWP support, a piece of 5×5 cm^2 conductive tape is attached to create a zero load. For the HWP support, no load is added.

4.1.3 Power Management Circuit. The power management circuit provides periodic voltage changes to the capacitor. As shown in Fig. 11c, the circuit consists of two switches, U1 and U4, for capacitor charging and discharging, respectively. When the charging enabling signal, EN, is activated, the charging path from VIN to VOUT is turned on via switch U1, and the external power source charges the capacitor. When EN is inactive, the discharging path from VOUT is turned on via switch U4, and the capacitor is connected to the ground for discharge. When the voltage level of the capacitor is lower than a predefined threshold, the discharging path is turned off to keep the low voltage level of the capacitor for signal modulation. The voltage threshold is determined by the varactor VR1, and the voltage comparison logic is achieved by the comparator U3 and the NOR gate U2.

4.2 3D Printing Retroreflector

We use a commercial 3D printing service [77] and the Nylon 12 material to fabricate the flat-bottom Luneburg lens. A python script is implemented to translate the permittivity distribution of the lens to the model file used for 3D printing. Fig. 11d shows a 3D-printed retroreflector that consists of many unit-element crossing structures. The lens is about 94 mm in width and 90 mm in height. The lens price is about $200, with the material cost of about $20. The current commercial 3D printing services are mainly for printing daily objects instead of high-resolution mmWave components. So the printing resolution is relatively low (around 0.8 mm). We thus set the rod size c of the elemental structure (Fig. 8a) to 1 mm and the cube size a to 3.6 mm. With this cube size, the lens printed by the commercial service only has a cutoff frequency of 26 GHz. Nonetheless, printing smaller cube sizes to support higher frequency is feasible [36, 42, 90, 92], and already supported by some commercial 3D printers [22, 76] with tens of μm resolution, which is more than enough

Frequency/f (GHz)	24	60	77
Bandwidth/B (GHz)	0.25	3.52	3.66
Chirp duration (ms)		0.1	
Tx power/P_t (dBm)	5	14	12
Tx gain/$G_t = G_{ts} + G_{ta}$ (dB)	13.5+3	5+15	12+3
Rx gain/$G_r = G_{rs} + G_{ra}$ (dB)	13.5+6	5+15	15+6
Processing Gain (dB)		27	

Table 1: Key parameters of experimental devices.

for UNISCATTER (*e.g.*, 0.3 mm at 77 GHz).

5 EVALUATION

5.1 Experimental Setup

We fabricate UNISCATTER following the process in Sec. 4 and conduct field tests in an outdoor parking lot, as shown in Fig. 12a. Fig. 12b shows the setup of the representative automotive driving scenario, where we mount a UNISCATTER tag on a tripod to emulate an intelligent road sign. Fig. 12c shows a complete assembly of the UNISCATTER tag. Specifically, the flat-bottom Luneburg lens retroreflector is placed in front of the capacitor and on the holder. The graphene capacitor (Fig. 11a) is placed at the front side of the support, aligning to the marker there (Fig. 11b). The cathode and anode of the graphene capacitor connect to the output ports, *i.e.*, VOUT and GND, of the power management circuit (Fig. 11c). An Arduino Due [5] supplies the power and sends binary modulation signals to the graphene capacitor. The switching rate of the graphene modulator is set to 100 Hz, and the duration of each modulation symbol is 50 ms, which leads to a Doppler frequency resolution of 20 Hz and a bitrate of 20 bps.

We mount a 24 GHz radar [34] on a sedan to conduct moving experiments. Besides, we also test the graphene modulator with a 77 GHz TI radar [81], and a 60 GHz JCAS device [31] from QualComm. The JCAS device reuses an existing 802.11ad/ay communication system as a radar sensor and provides CIR measurements to decode UNISCATTER signals (Sec. 3.3). Tab. 1 summarizes the parameters of the experimental devices. The Tx/Rx gain G_x consists of the single antenna gain G_{xs} and the antenna array gain $G_{xa} = 10\log_{10}N_x$, where N_x is the number of Tx/Rx antennas. In addition, we use $N_c = 500$ chirps to calculate each Doppler spectrum, which provides an additional processing gain of $10\log_{10}N_c = 27$dB.

During the experiments, we record the RSS and the noise floor at the receiver (within the tag's modulation band) and derive the SNR. Then we can calculate the SNR and estimate the modulated bit-error rate (BER). Specifically, as UNISCATTER adopts FSK, its BER $= \frac{1}{2}\text{erfc}(\sqrt{\frac{\text{SNR}}{8}})$. For example, an SNR of 10 dB corresponds to a raw BER of 5.7%.

Given the RSS, we can estimate the differential RCS of the tag using the device parameters (Tab. 1) and the radar equation (Eq. 1). In contrast, directly measuring the RCS of the tag requires sophisticated equipment, e.g., an anechoic chamber for the retroreflector and a mmWave vector network analyzer for the modulator. Hence, we leave the accurate characterization of individual components as future work.
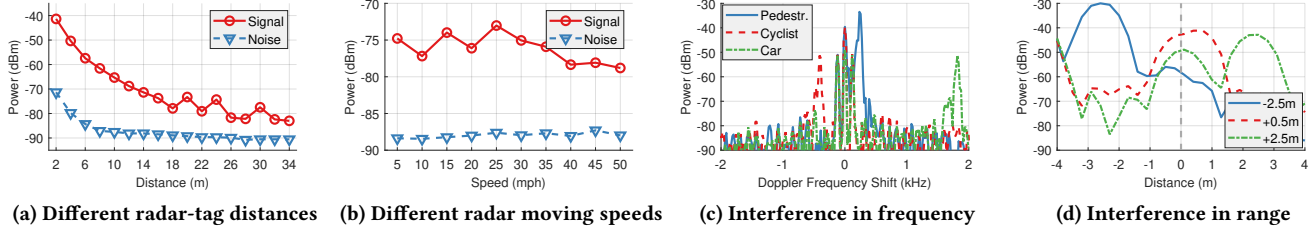
(a) Different radar-tag distances (b) Different radar moving speeds (c) Interference in frequency (d) Interference in range

Figure 13: Performance of tag detection.

5.2 Performance of Tag Detection

Detection distance. To measure the tag detection range, we move the radar along the broadside direction of the tag. Fig. 13a shows the RSS and noise at sampled locations. The RSS decreases from -41 dBm to -83 dBm as distance increases from 2 m to 34 m, roughly following the free-space path loss model with a few exceptions. The possible reasons for the outliers are multipath reflections from the ground or radar tilting due to bumpy ground. Meanwhile, the noise floor of the radar dramatically decreases from -70 dBm to -85 dBm when the distance is less than 6 m, and gradually decreases below -90 dBm thereafter. The high noise at short distances is due to the harmonics generated from the FSK modulation of the tag. The gradually decreasing noise partially compensates for the increased free-space path loss. Overall, UNIS-CATTER can communicate at a maximum distance of around 30 m, with SNR over 10 dB and corresponding BER lower than 5.7%. Additional coding (*e.g.*, BCH code) can be applied to correct the bit errors. We expect this suffices for typical use cases such as smart roadside infrastructures.

Impact of radar mobility. To represent a mobile scenario, we repetitively drive the sedan at various speeds from 5 mph to 50 mph, and sample the RSS and noise when the vehicle is about 10 m away from the tag. As shown in Fig. 13b, the RSS remains at around -75 dBm when the speed is lower than 30 mph and gradually decreases as the speed increases. The RSS degradation at high speed is mainly due to the spreading effect of the Doppler frequency shift. Specifically, since the tag is not straight in the moving direction of the radar, its Doppler frequency offset drifts even if the vehicle moves at a constant speed. As a result, the width of the peaks in the Doppler frequency spectrum increases, and the peak power decreases. Nonetheless, UNISCATTER still achieves an acceptable SNR of 10 dB at 50 mph.

Impact of environmental interferences. Traffic occasionally around the tag may cause interference. To evaluate its impact, we let common traffic, such as cars, cyclists, and pedestrians, pass by the tag. We find that the interference only occurs when moving objects are very close to the tag, where the radar cannot separate them in its range spectrum. Fig. 13c shows the Doppler spectrum when objects just pass by the tag. Each moving object creates a dominant peak in the Doppler frequency spectrum. When objects move at high speed, such as vehicles and cyclists, their Doppler frequency shifts are very different from the coding peaks of the tag, so that the radar can still detect the coding pattern. However,

when the Doppler frequency shift of the object is close to the coding frequency, such as a pedestrian, the coding pattern is distorted and cannot be correctly detected. Nonetheless, the interference caused by the objects passing by is transient and can be overcome with a longer observation period.

Then, we evaluate the interference when pedestrians cross the road, so that they may block the tag or create background reflections. Fig. 13d shows the range spectrum when the pedestrian is at different distances from the tag. A negative distance (*e.g.*-2.5m) means that the pedestrian blocks the tag, where the radar fails to detect the tag due to blockage. Such blockage can be easily avoided by lifting the tag and exploiting the wide elevation coverage of the tag. In contrast, when the pedestrian is behind the tag, it hardly impacts the coding pattern. When the pedestrian is very close to the tag (*i.e.* +0.5 m), although the radar cannot separate the pedestrian from the tag, the pedestrian creates a near-zero Doppler frequency shift only, and the coding pattern of the tag remains unchanged.

The analysis of moving objects also applies to possibly co-located tags. When multiple co-located tags cannot be separated by the radar, the tags need to be configured in time or frequency division multiplexing modes. TDM requires synchronizing tags, which is feasible when tags are co-located and share a controller. FDM requires a wide modulation bandwidth to achieve higher modulation rates, whose potential solutions are discussed in Sec. 6.

5.3 Performance of Tag Coverage

The flat-bottom Luneburg lens is designed to achieve an angular coverage of 70 ° in both azimuth and elevation. To test its actual coverage when combined with the graphene modulator, we use a laser level and a protractor to align the tag at the broadside direction of the radar and rotate the tag, which effectively varies its directions relative to the radar.

Azimuth coverage. Fig. 14a shows that, with the lens, the RSS increases and then decreases slightly as the azimuth angle increases from 0° to 35°. The RSS change near the broadside direction matches the simulated monostatic RCS pattern (Fig. 7d). At larger azimuth angles, the RSS degradation may be due to the partial blockage of the stand. In contrast, without the lens, only the RSS at the broadside direction is as high as that with the lens. As the tag slightly deviates from the broadside, the RSS drops dramatically by about 25 dB. The RSS rises again as the azimuth angle further increases because a corner reflector is formed by the
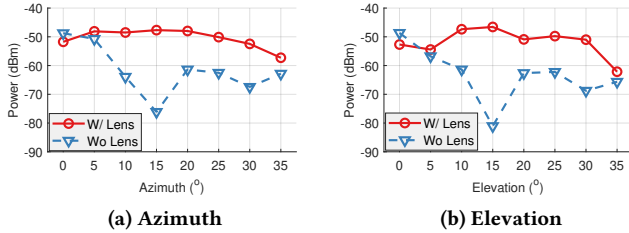
(a) Azimuth **(b) Elevation**

Figure 14: Performance of retroreflector.

graphene capacitor and the side wall of the stand. Nonetheless, the RSS with the lens is still more than 10 dB higher.

Elevation coverage. To measure the elevation coverage, we rotate the UniScatter tag vertically by 90 ° and repeat the above experiment. Fig. 14b shows the RSS at different elevation angles. Similar to the azimuth direction, the lens has an elevation coverage of about 70°, which matches the specs by design. The RSS drops by around 10 dB as the angle increases from 30° to 35°. This may be due to the fabrication inaccuracy of the 3D printer. In contrast, the RSS without the lens is similar to that along the azimuth direction. These two experiments together verify the effectiveness of the flat-bottom Luneburg lens design.

Although we cannot directly measure the RCS of the lens, we are still able to estimate the loss of the lens based on Fig. 14. By comparing the RSS with and without the lens at 0°, we observe a loss of about 3 dB, which is due to fabrication inaccuracy and dissipation in dielectric materials.

5.4 Performance of Tag Coding

To evaluate the graphene modulator, we place the tag in the broadside direction of the radar, and vary its switching rate from 0.1 Hz to 500 Hz.

Effectiveness of metal coating. We first verify the impact of the metal coating design on the modulation efficiency. Fig. 15a shows that the RSS decreases with the switching rate since the graphene capacitor is less likely to be fully charged with a shorter charging cycle. As a result, the actual bias voltage between the graphenes is smaller than the designed voltage, resulting in a smaller $\Delta\Gamma$. When the switching rate goes above 10 Hz, the metal-coated modulator experiences a much lower RSS dropping rate than the default modulator. At 100 Hz switching rate, the coated modulator outperforms the default by 7 dB. These results demonstrate the necessity and effectiveness of the metal coating.

Impact of support configuration. We then evaluate the performance of the modulator with different support configurations. We fabricate the QWP and HWP according to Sec. 3.1.2 and evaluate their performance with different switching rates. As shown in Fig. 15b, the two support configurations have similar RSS decrease trends as the switching rate increases. It indicates that the RSS drop is an intrinsic property of the graphene capacitor. Meanwhile, the RSS of the HWP is consistently lower than that of the QWP by about 5 dB, which matches the theoretical difference of $\Delta\Gamma$ between QWP and HWP (Fig. 3a).

Impact of operating frequency. Finally, we evaluate the performance of the modulator (with QWP) at different operating frequencies, using the aforementioned 24 GHz and 77 GHz automotive radars and the 60 GHz JCAS device. As stated in Sec. 4.2, the lens currently fabricated only supports frequencies lower than 26 GHz, due to the fabrication limitation of the 3D printer used. Thus, we remove the lens and put the RF devices in the broadside direction of the tag. Since the radar sensing hardware have different hardware configurations, *e.g.*, transmit power, noise figures, bandwidth, array aperture size, antenna gain, *etc.*, we only report the SNR metric, as shown in Fig. 15c. The RSS variation trends are similar across the three devices, indicating that the modulator works consistently across an extremely wide mmWave band. Despite the different hardware configurations, UniScatter achieves similar SNRs of about 47 dB, 38 dB, and 46 dB at 24 GHz, 60 GHz, and 77 GHz, respectively, at 2 m. The comparable SNR between the 24 GHz and 77 GHz is mainly because the RCS of UniScatter scales with $\frac{1}{\lambda^2}$, which compensates for the increased path loss proportional to λ^2. The lower SNR at 60 GHz is partly because the $\Delta\Gamma$ at 60 GHz is smaller than that at other frequencies, with the QWP (Fig. 3b). The results show that similar detection distances will be achieved at 24 GHz and 77 GHz, and a shorter distance with a factor of 0.6 is achieved at 60 GHz.

5.5 Reliability against Environment

One key advantage of RF sensing is that it is robust under adverse weather and lighting conditions, which is important for vehicular use cases. To showcase such scenarios, we use a heavy-duty fog effect generator to emulate fog and conduct measurements during day and night. To emulate a light fog, we generate the fog intermittently and let the fog disperse in the space. For a heavy fog, we keep generating the fog so that it remains dense. Fig. 16 shows that the weather and lighting conditions have almost no impact on the RSS of the tag, demonstrating the robustness of UniScatter.

5.6 Impact of Device Configuration

In practice, mmWave sensing devices such as radar usually avoid fully using their entire bandwidth and large array aperture, in order to reduce data transferring and computation overhead. We evaluate the impact of such hardware parameters and identify key factors for further improving UniScatter's performance.

Bandwidth. We configure the 24 GHz radar to operate with different bandwidths from 50 MHz to 250 MHz, with a fixed number of samples per chirp. Fig. 17a shows that, both the RSS and noise floor increase proportionally with bandwidth. Consequently, the SNR remains constant, indicating that a large radar sensing bandwidth cannot improve the performance of UniScatter.
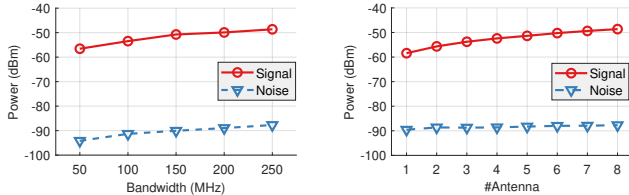
Antenna array size. To evaluate the impact of array aperture size, we configure the radar to use different numbers of Tx-Rx antenna pairs from 1 to 8. As shown in Fig. 17b, the
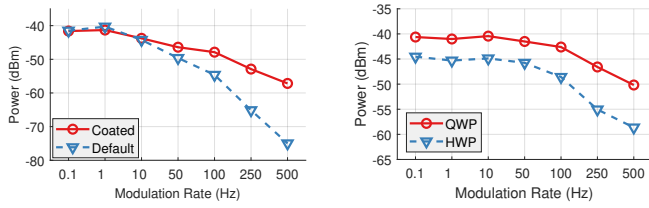
(a) Impact of metal coating   (b) Different structures   (c) Different frequencies

Figure 15: Performance of graphene modulator.

Figure 16: Weather and lighting conditions.

(a) Bandwidth   (b) Antenna array size

Figure 17: Impact of Radar configuration.

tag RSS increases proportionally with the number of antenna pairs, while the noise remains almost invariant. So the SNR of UniScatter can be significantly improved with multi-antenna radar, leading to a more extended communication distance or a smaller BER.

6 DISCUSSION AND FUTURE WORK

Higher switching rate. A higher switching rate can increase the maximum data rate, and make the UniScatter more robust against the Doppler spreading effect in dynamic scenarios. However, a higher switching rate also increases the spacing between the coding peaks and the carrier peak in the Doppler frequency spectrum. These coding peaks may be recognized as fake objects by legacy radars without the backscatter communication function, and pose safety and security risks. The modulation rate of our current UniScatter prototype is 100 Hz, but it can be further improved in two ways. First, the gap size of the graphene capacitor can be reduced to improve the response time of the capacitor. Second, the graphene capacitor can be replaced by other graphene-based components with potentially faster responses, such as graphene transistor [27]. We leave the exploration of such mechanisms as future work.

Longer detection distance. The detection distance of UniScatter mainly depends on the RSS of the coding peaks, which can be improved in two ways according to Eq. (2). First, a larger lens leads to a larger RCS of the tag. For example, increasing the lens size of UniScatter from 10 cm to 20 cm can further extend the detection distance from 30 m to 60 m. Second, a higher switching rate leads to a larger $\Delta\Gamma$, which can also translate into a longer distance.

Smaller tag size. The size of UniScatter is limited by the detection distance, as discussed above. Nonetheless, it is noted that only the transverse area of the lens determines the received signal power and hence the maximum distance of the tag. Thus, we can thin the lens along the longitudinal
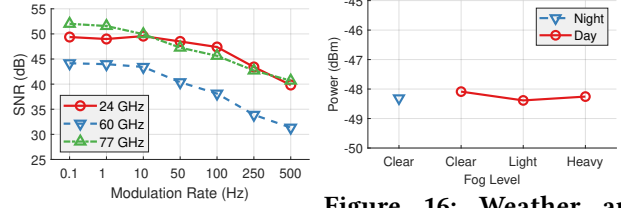
axis (z-axis in Fig. 7) by transforming the original spherical lens into a cylindrical flat lens. With a smaller lens volume, larger permittivity is required to properly refract signals, which can be achieved using 3D printing ceramics [55].

Low power consumption. The power consumption of UniScatter is about 50 mW at the switching rate of 100 Hz, mainly due to the large capacitance of the graphene capacitor. Two main factors contribute to capacitance. First, the power consumption is proportional to the size of the capacitor. UniScatter has a large 5×5 cm^2 capacitor area to achieve $70°$ coverage along both azimuth and elevation directions. In practice, the shape of the graphene capacitor can be customized based on the coverage requirement. For example, an intelligent road sign needs wide azimuth coverage but narrow elevation coverage while a traffic light vice versa. Thus, a thin and long graphene capacitor can be used to reduce power consumption dramatically. Second, we find that the metal coating consumes much power but does not contribute to $\Delta\Gamma$. We believe more advanced fabrication techniques can isolate the metal coating from the electrolyte and thus reduce power consumption. Besides, the capacitor size can be reduced by further shrinking the flat area of the lens using the TO technique. Finally, new tuning mechanisms with lower power consumption, *e.g.*, graphene transistor [27], can potentially replace the graphene capacitor. We leave such power optimization mechanisms for future work.

7 CONCLUSION

We have designed, fabricated, and validated UniScatter, a metamaterial-based mmWave tag for multi-frequency mmWave backscattering. We explore the design space of the retrore-flector and the modulator of a mmWave backscatter tag and propose a novel backscatter tag architecture for the mmWave band. UniScatter can communicate with not only mmWave radar, but also communication-centric JCAS devices such as WiGig and potentially 5G. UniScatter can accommodate a wide range of use cases such as intelligent transportation and information kiosks.

REFERENCES

[1] Aftab Ahmed, Irene A Goldthorpe, and Amir K Khandani. 2015. Electrically tunable materials for microwave applications. *Applied Physics Reviews* 2, 1 (2015).

[2] Khalid Aljonubi, Ahmed O AlAmoudi, Richard J Langley, and Ian Reaney. 2013. Reconfigurable antenna using smart material. In *Proceedings of IEEE EuCAP*.

[3] Paris Ang, Gengyu Xu, and George V Eleftheriades. 2021. Invisibility cloaking with passive and active Huygens's metasurfaces. *Applied Physics Letters* 118, 7 (2021).

[4] Ansys. [n.d.]. HFSS. https://www.ansys.com/products/electronics/ansys-hfss.

[5] Arduino. [n.d.]. Arduino Due. https://store-usa.arduino.cc/products/arduino-due.

[6] Venkat Arun and Hari Balakrishnan. 2020. {RFocus}: Beamforming Using Thousands of Passive Antennas. In *Proceedings of USENIX NSDI*.

[7] Kang Min Bae, Namjo Ahn, Yoon Chae, Parth Pathak, Sung-Min Sohn, and Song Min Kim. 2022. OmniScatter: extreme sensitivity mmWave backscattering using commodity FMCW radar. In *Proceedings of ACM MobiSys*.

[8] Ryan A Bahr, Ajibayo O Adeyeye, Samantha Van Rijs, and Manos M Tentzeris. 2020. 3D-printed omnidirectional Luneburg lens retroreflectors for low-cost mm-wave positioning. In *Proceedings of IEEE International Conference on RFID*.

[9] Constantine A Balanis. 2015. *Antenna theory: analysis and design*. John wiley & sons.

[10] Osman Balci, Nurbek Kakenov, and Coskun Kocabas. 2017. Controlling phase of microwaves with active graphene surfaces. *Applied Physics Letters* 110, 16 (2017).

[11] BioLogic. [n.d.]. SP-200 Potentiostat. https://www.biologic.net/products/sp-200.

[12] Soumitra Biswas and Mark Mirotznik. 2020. High gain, wide-angle QCTO-enabled modified Luneburg lens antenna with broadband anti-reflective layer. *Scientific reports* 10, 1 (2020).

[13] Anders Bondeson, Thomas Rylander, and Pär Ingelström. 2012. *Computational electromagnetics*. Springer.

[14] Michael Boyarsky, Timothy Sleasman, Mohammadreza F Imani, Jonah N Gollub, and David R Smith. 2021. Electronically steered metasurface antenna. *Scientific reports* 11, 1 (2021).

[15] Yoon Chae, Kang Min Bae, Parth Pathak, and Song Min Kim. 2020. On the Feasibility of Millimeter-wave Backscatter using Commodity 802.11 ad 60 GHz Radios. In *Proceedings of ACM WiNTECH*.

[16] CheapTubes. [n.d.]. Monolayer graphene on copper foil. https://www.cheaptubes.com/product/monolayer-graphene-copper-foil-6-x-6-150-mm-x-150-mm.

[17] Lili Chen, Wenjun Hu, Kyle Jamieson, Xiaojiang Chen, Dingyi Fang, and Jeremy Gummeson. 2021. Pushing the Physical Limits of {IoT} Devices with Programmable Metasurfaces. In *Proceedings of USENIX NSDI*.

[18] Xudong Chen, Tomasz M Grzegorczyk, Bae-Ian Wu, Joe Pacheco Jr, and Jin Au Kong. 2004. Robust method to retrieve the constitutive effective parameters of metamaterials. *Physical review E* 70, 1 (2004).

[19] HD Eckhardt. 1971. Simple model of corner reflector phenomena. *Applied Optics* 10, 7 (1971).

[20] Aline Eid, Jimmy GD Hester, and Manos M Tentzeris. 2020. Rotman lens-based wide angular coverage and high-gain semipassive architecture for ultralong range mm-wave rfids. *IEEE Antennas and Wireless Propagation Letters* 19, 11 (2020), 1943–1947.

[21] Senglee Foo. 2017. Liquid-crystal-tunable metasurface antennas. In *Proceedings of IEEE EuCAP*.

[22] Formlabs. [n.d.]. Form 3+. https://formlabs.com/uk/3d-printers/form-3.

[23] Chuhan Gao, Yilong Li, and Xinyu Zhang. 2018. {LiveTag}: Sensing {Human-Object} Interaction through Passive Chipless {WiFi} Tags. In *Proceedings of USENIX NSDI*.

[24] Reza Ghaffarivardavagh, Sayed Saad Afzal, Osvy Rodriguez, and Fadel Adib. 2020. Ultra-wideband underwater backscatter via piezoelectric metamaterials. In *Proceedings of ACM SIGCOMM*.

[25] Sandeep Gogineni, Muralidhar Rangaswamy, Joseph R Guerci, Jamie S Bergin, and David R Kirk. 2019. Estimation of radar channel state information. In *Proceedings of IEEE RadarConf*.

[26] Xiuzhen Guo, Longfei Shangguan, Yuan He, Nan Jing, Jiacheng Zhang, Haotian Jiang, and Yunhao Liu. 2022. Saiyan: Design and Implementation of a Low-power Demodulator for {LoRa} Backscatter Systems. In *Proceedings of USENIX NSDI*.

[27] Yire Han, Byeong-Ju Park, Ji-Ho Eom, Venkatraju Jella, Swathi Ippili, SVN Pammi, Jin-Seok Choi, Hyunwoo Ha, Hyuk Choi, Cheolho Jeon, et al. 2021. Direct Growth of Highly Conductive Large-Area Stretchable Graphene. *Advanced Science* 8, 7 (2021).

[28] Qiong He, Shulin Sun, and Lei Zhou. 2019. Tunable/reconfigurable metasurfaces: physics and applications. *Research* 2019 (2019).

[29] Mehrdad Hessar, Ali Najafi, and Shyamnath Gollakota. 2019. {NetScatter}: Enabling {Large-Scale} Backscatter Networks. In *Proceedings of USENIX NSDI*.

[30] Jimmy GD Hester and Manos M Tentzeris. 2017. A mm-wave ultra-long-range energy-autonomous printed rfid-enabled van-atta wireless sensor: At the crossroads of 5g and iot. In *Proceedings of IEEE MTT-S IMS*.

[31] Eran Hof, Amichai Sanderovich, and Evyatar Hemo. 2020. Face Verification Using 60~ GHz 802.11 waveforms. *arXiv preprint arXiv:2002.11965* (2020).

[32] Jin Hu, Xiaoming Zhou, and Gengkai Hu. 2009. Design method for electromagnetic cloak with arbitrary shapes based on Laplace's equation. *Optics express* 17, 3 (2009).

[33] John Hunt, Nathan Kundtz, Nathan Landy, Vinh Nguyen, Tim Perram, Anthony Starr, and David R Smith. 2011. Broadband wide angle lens implemented with dielectric metamaterials. *Sensors* 11, 8 (2011).

[34] INRAS. [n.d.]. Radarbook2. https://inras.at/en/radarbook2.

[35] Yongtao Jia, Ying Liu, Wenbo Zhang, and Shuxi Gong. 2016. Ultra-wideband and high-efficiency polarization rotator based on metasurface. *Applied physics letters* 109, 5 (2016).

[36] Petr Kadera and Jaroslav Lacik. 2021. Performance comparison of W-band Luneburg lens antenna: additive versus subtractive manufacturing. In *Proceedings of IEEE COMITE*.

[37] Bryce Kellogg, Aaron Parks, Shyamnath Gollakota, Joshua R Smith, and David Wetherall. 2014. Wi-Fi backscatter: Internet connectivity for RF-powered devices. In *Proceedings of ACM SIGCOMM*.

[38] Keysight. [n.d.]. PathWave EM Design (EMPro). https://www.keysight.com/us/en/products/software/pathwave-design-software/pathwave-em-design-software.html.

[39] Md Khan, Abdul Kaium, Md Ullah, Rifat Kabir, Mohammad Abdul Alim, et al. 2020. High-performance graphene patch antenna with superstrate cover for terahertz band application. *Plasmonics* 15, 6 (2020).

[40] John Kimionis, Apostolos Georgiadis, Spyridon Nektarios Daskalakis, and Manos M Tentzeris. 2021. A printed millimetre-wave modulator and antenna array for backscatter communications at gigabit data rates. *Nature Electronics* 4, 6 (2021).

[41] Preeti Kumari, Junil Choi, Nuria González-Prelcic, and Robert W Heath. 2017. IEEE 802.11 ad-based radar: An approach to joint vehicular communication-radar system. *IEEE Transactions on Vehicular Technology* 67, 4 (2017).

[42] Zachary Larimore, Sarah Jensen, Austin Good, Aric Lu, John Suarez, and Mark Mirotznik. 2018. Additive manufacturing of Luneburg lens antennas using space-filling curves and fused filament fabrication. *IEEE transactions on antennas and propagation* 66, 6 (2018).

[43] Antonio Lazaro, Marc Lazaro, Ramon Villarino, David Girbau, and Pedro de Paco. 2021. Car2car communication using a modulated backscatter and automotive fmcw radar. *Sensors* 21, 11 (2021).

[44] Chengfan Li, Junjuan Zhao, Jingyuan Yin, Guifan Zhang, and Xinjian Shan. 2010. Analysis of RCS characteristic of dihedral corner and triangular trihedral corner reflectors. In *Proceedings of IEEE ICCSE*.

[45] Quan Li, Zhen Tian, Xueqian Zhang, Ranjan Singh, Liangliang Du,

Jianqiang Gu, Jiaguang Han, and Weili Zhang. 2015. Active graphene–silicon hybrid diode for terahertz waves. *Nature communications* 6, 1 (2015).

[46] Yujian Li, Lei Ge, Meie Chen, Zhan Zhang, Zheng Li, and Junhong Wang. 2019. Multibeam 3-D-printed Luneburg lens fed by magneto-electric dipole antennas for millimeter-wave MIMO applications. *IEEE Transactions on Antennas and Propagation* 67, 5 (2019).

[47] Ying Li and Qi Zhu. 2016. Luneburg lens with extended flat focal surface for electronic scan applications. *Optics express* 24, 7 (2016).

[48] Zhengxiong Li, Baicheng Chen, Kun Wang, and Wenyao Xu. 2021. FerroTag: When Inkables Meet Wireless Signals. *GetMobile: Mobile Computing and Communications* 24, 3 (2021).

[49] Zeyan Li, Bo Li, Qian Zhao, and Ji Zhou. 2020. A metasurface absorber based on the slow-wave effect. *AIP Advances* 10, 4 (2020).

[50] Min Liang, Wei-Ren Ng, Kihun Chang, Kokou Gbele, Michael E Gehm, and Hao Xin. 2014. A 3-D Luneburg lens antenna fabricated by polymer jetting rapid prototyping. *IEEE Transactions on Antennas and Propagation* 62, 4 (2014).

[51] Fan Liu and Christos Masouros. 2019. Hybrid beamforming with sub-arrayed MIMO radar: Enabling joint sensing and communication at mmWave band. In *Proceedings of IEEE ICASSP*.

[52] Fan Liu, Longfei Zhou, Christos Masouros, Ang Li, Wu Luo, and Athina Petropulu. 2018. Toward dual-functional radar-communication systems: Optimal waveform design. *IEEE Transactions on Signal Processing* 66, 16 (2018).

[53] Vincent Liu, Aaron Parks, Vamsi Talla, Shyamnath Gollakota, David Wetherall, and Joshua R Smith. 2013. Ambient backscatter: Wireless communication out of thin air. *Proceedings of ACM SIGCOMM* 43, 4 (2013).

[54] Vincent Liu, Vamsi Talla, and Shyamnath Gollakota. 2014. Enabling instantaneous feedback with full-duplex backscatter. In *Proceedings of ACM MobiCom*.

[55] Yi-Hui Lou, Ya-Xin Zhu, Gui-Fen Fan, Wen Lei, Wen-Zhong Lu, and Xiao-Chuan Wang. 2020. Design of Ku-band flat luneburg lens using ceramic 3-D printing. *IEEE Antennas and Wireless Propagation Letters* 20, 2 (2020), 234–238.

[56] RK Luneberg. 1944. *Mathematical Theory of Optics. Providence.* RI: Brown Univ. Press.

[57] Yunfei Ma, Nicholas Selby, and Fadel Adib. 2017. Minding the billions: Ultra-wideband localization for deployed rfid tags. In *Proceedings of ACM MobiCom*.

[58] Holger Maune, Matthias Jost, Roland Reese, Ersin Polat, Matthias Nickel, and Rolf Jakoby. 2018. Microwave liquid crystal technology. *Crystals* 8, 9 (2018).

[59] Mohammad Hossein Mazaheri, Alex Chen, and Omid Abari. 2021. mmTag: a millimeter wave backscatter network. In *Proceedings of ACM SIGCOMM*.

[60] Ziqi Miao, Qiong Wu, Xin Li, Qiong He, Kun Ding, Zhenghua An, Yuanbo Zhang, and Lei Zhou. 2015. Widely tunable terahertz phase modulation with gate-controlled graphene metasurfaces. *Physical Review X* 5, 4 (2015), 041027.

[61] Graeme W Milton, Marc Briane, and John R Willis. 2006. On cloaking for elasticity and physical equations with a transformation invariant form. *New journal of physics* 8, 10 (2006).

[62] Kumar Vijay Mishra, MR Bhavani Shankar, Visa Koivunen, Bjorn Ottersten, and Sergiy A Vorobyov. 2019. Toward millimeter-wave joint radar communications: A signal processing perspective. *IEEE Signal Processing Magazine* 36, 5 (2019).

[63] Carl Mungan. 2001. The cat's eye retroreflector.

[64] John Nolan, Kun Qian, and Xinyu Zhang. 2021. RoS: passive smart surface for roadside-to-vehicle communication. In *Proceedings of ACM SIGCOMM*.

[65] Yao Peng, Longfei Shangguan, Yue Hu, Yujie Qian, Xianshang Lin, Xiaojiang Chen, Dingyi Fang, and Kyle Jamieson. 2018. PLoRa: A passive long-range data network from ambient LoRa transmissions. In *Proceedings of ACM SIGCOMM*.

[66] PiezoDirect. [n.d.]. Circular Piezo Ceramic Actuators. https://

piezodirect.com/piezo-disc-actuators.

[67] Y. Poplavko, Y. Prokopenko, V. Pashkov, V. Molchanov, I. Golubeva, V. Kazmirenko, and D. Smigin. 2006. Low Loss Microwave Piezo-Tunable Devices. In *Proceedings of IEEE EuMC*.

[68] Kun Qian and Xinyu Zhang. 2022. MilliMirror: 3D Printed Reflecting Surface for Millimeter-Wave Coverage Expansion. In *Proceedings of ACM MobiCom*.

[69] Hermann Rohling, Steffen Heuel, and Henning Ritter. 2010. Pedestrian detection procedure integrated into an 24 GHz automotive radar. In *Proceedings of IEEE RADAR*.

[70] Carl W Rossler, Emre Ertin, and Randolph L Moses. 2011. A software defined radar system for joint communication and sensing. In *Proceedings of IEEE RADAR*.

[71] Mahdi Safari, Yuchu He, Minseok Kim, Nazir P Kherani, and George V Eleftheriades. 2020. Optically and radio frequency (RF) transparent meta-glass. *Nanophotonics* 9, 12 (2020).

[72] D Schurig, JB Pendry, and David R Smith. 2006. Calculation of material properties and ray tracing in transformation media. *Optics express* 14, 21 (2006).

[73] E Sharp and M Diab. 1960. Van Atta reflector array. *IRE Transactions on Antennas and Propagation* 8, 4 (1960).

[74] Abhay Shivayogimath, Patrick Rebsdorf Whelan, David MA Mackenzie, Birong Luo, Deping Huang, Da Luo, Meihui Wang, Lene Gammelgaard, Haofei Shi, Rodney S Ruoff, et al. 2019. Do-it-yourself transfer of large-area graphene using an office laminator and water. *Chemistry of Materials* 31, 7 (2019).

[75] Elahe Soltanaghaei, Akarsh Prabhakara, Artur Balanuta, Matthew Anderson, Jan M Rabaey, Swarun Kumar, and Anthony Rowe. 2021. Millimetro: mmWave retro-reflective tags for accurate, long range localization. In *Proceedings of ACM MobiCom*.

[76] Stratasys. [n.d.]. Objet30 3D Printer. https://www.stratasys.com/en/3d-printers/printer-catalog/objet30-printer.

[77] Stratasys. [n.d.]. Stratasys Direct Manufacturing. https://www.stratasys.com/en/stratasysdirect.

[78] Axel Strobel, Christian Carlowitz, Robert Wolf, Frank Ellinger, and Martin Vossiek. 2013. A millimeter-wave low-power active backscatter tag for FMCW radar systems. *IEEE transactions on microwave theory and techniques* 61, 5 (2013).

[79] Xin Tan, Zhi Sun, Dimitrios Koutsonikolas, and Josep M Jornet. 2018. Enabling indoor mobile millimeter-wave networks based on smart reflect-arrays. In *Proceedings of IEEE INFOCOM*.

[80] Temescal. [n.d.]. BJD 1800 E-Beam Evaporator. https://www.capovani.com/iinfo.cfm?itemno=87979.

[81] TexasInstrument. [n.d.]. AWR1243BOOST. https://www.ti.com/tool/AWR1243BOOST.

[82] Jeremiah P Turpin, Jeremy A Bossard, Kenneth L Morgan, Douglas H Werner, and Pingjuan L Werner. 2014. Reconfigurable and tunable metamaterials: a review of the theory and applications. *International Journal of Antennas and Propagation* 2014 (2014).

[83] Anran Wang, Vikram Iyer, Vamsi Talla, Joshua R Smith, and Shyamnath Gollakota. 2017. {FM} backscatter: Enabling connected cities and smart fabrics. In *Proceedings of USENIX NSDI*.

[84] Hai Wang, Hao Liang, and Zhengfang Qian. 2020. Tunable Conductivity and Dielectric Constant of Graphene in Microwave, Millimeter wave and Terahertz Band. In *Proceedings of IEEE UCMMT*.

[85] Thorsten Wild, Volker Braun, and Harish Viswanathan. 2021. Joint design of communication and sensing for beyond 5G and 6G systems. *IEEE Access* 9 (2021).

[86] Chenshu Wu, Feng Zhang, Beibei Wang, and KJ Ray Liu. 2020. mm-Track: Passive multi-person localization using commodity millimeter wave radio. In *Proceedings of IEEE INFOCOM*.

[87] Mingmao Wu, Fengyao Chi, Hongya Geng, Hongyun Ma, Miao Zhang, Tiantian Gao, Chun Li, and Liangti Qu. 2019. Arbitrary waveform AC line filtering applicable to hundreds of volts based on aqueous electrochemical capacitors. *Nature communications* 10, 1 (2019).

[88] Yang Wu, Chan La-o vorakiat, Xuepeng Qiu, Jingbo Liu, Praveen Deorani, Karan Banerjee, Jaesung Son, Yuanfu Chen, Elbert EM Chia,

and Hyunsoo Yang. 2015. Graphene terahertz modulators by ionic liquid gating. *Advanced Materials* 27, 11 (2015), 1874–1879.

[89] Dianhan Xie, Xudong Wang, and Aimin Tang. 2022. MetaSight: localizing blocked RFID objects by modulating NLOS signals via metasurfaces. In *Proceedings of ACM MobiSys*.

[90] Hao Xin and Min Liang. 2017. 3-D-printed microwave and THz devices using polymer jetting techniques. *Proc. IEEE* 105, 4 (2017).

[91] Pouria Yaghmaee, Onur Hamza Karabey, Bevan Bates, Christophe Fumeaux, and Rolf Jakoby. 2013. Electrically tuned microwave devices using liquid crystal technology. *International Journal of Antennas and Propagation* 2013 (2013).

[92] Huan Yi, Shi-Wei Qu, Kung-Bo Ng, Chi Hou Chan, and Xue Bai. 2015. 3-D printed millimeter-wave and terahertz lenses with fixed and fre-quency scanned beam. *IEEE Transactions on Antennas and Propagation* 64, 2 (2015).

[93] Chao Zeng, Xueming Liu, and Guoxi Wang. 2014. Electrically tunable graphene plasmonic quasicrystal metasurfaces for transformation optics. *Scientific reports* 4, 1 (2014), 1–8.

[94] J Andrew Zhang, Md Lushanur Rahman, Kai Wu, Xiaojing Huang, Y Jay Guo, Shanzhi Chen, and Jinhong Yuan. 2021. Enabling joint communication and radar sensing in mobile networks—A survey. *IEEE Communications Surveys & Tutorials* 24, 1 (2021).

[95] Pengyu Zhang, Dinesh Bharadia, Kiran Joshi, and Sachin Katti. 2016. Hitchhike: Practical backscatter using commodity wifi. In *Proceedings of ACM SenSys*.